

Investigation of hygrothermal behavior of a novel bio-based panel: Experiment and numerical simulation

Yaping Zhou^{1,*}, Abdelkrim Trabelsi², Li Xiang¹, Mohamed El Mankibi³¹ School of Energy and Power Engineering, Changsha University of Science and Technology, Changsha 410114, Hunan Province, China² CETHIL, UCBL, University of Lyon, Villeurbanne 69622, France³ LTDS, ENTPE, University of Lyon, Vaulx-en-Velin 69120, France* Corresponding author: Yaping Zhou, zyaping@csust.edu.cn

CITATION

Zhou Y, Trabelsi A, Xiang L, El Mankibi M. Investigation of hygrothermal behavior of a novel bio-based panel: Experiment and numerical simulation. *Clean Energy Science and Technology*. 2025; 3(1): 249.
<https://doi.org/10.18686/cest249>

ARTICLE INFO

Received: 20 October 2024

Accepted: 23 December 2024

Available online: 2 January 2025

COPYRIGHT



Copyright © 2025 by author(s).

Clean Energy Science and Technology is published by Universe Scientific Publishing. This work is licensed under the Creative Commons Attribution (CC BY) license.
<https://creativecommons.org/licenses/by/4.0/>

Abstract: Straw composites, owing to their low carbon footprint and favorable hygrothermal properties, are becoming a promising alternative insulation material for buildings in order to promote energy saving and occupants' comfort. However, the heat and moisture characteristics of straw composites at the material scale and under steady-state condition are insufficient for a thorough assessment of their performance as a building component in actual service conditions. This study focused on the hygrothermal performance of a novel bio-based wall made with a rice straw–alginate composite material. The temperature and relative humidity profiles within the wall were monitored under various boundary conditions. The inverse analysis method was proposed to determine liquid water permeability. In a dynamic test, compared with the model of coupled heat-and-moisture transfer (CHM), the transient heat transfer model predicted temperature profiles with higher errors and underestimated total heat flux by up to 30.6%. Also, under the dynamic condition, the CHM model with liquid water transport showed decreased mean absolute errors by 61%, 57% and 8% at depths of 28 mm, 36 mm and 64 mm, respectively, compared with those predicted by the CHM model without liquid water transport. Both vapor transport and liquid transport seemed to be essential when modeling thermal transfer and moisture transfer through the wall.

Keywords: straw composite; hygroscopic material; liquid water permeability; coupled heat and moisture transfer; inverse parameter estimation

1. Introduction

The building sector is responsible for 30%–40% of total energy consumption and global greenhouse gas emissions [1], a substantial portion of which is directly associated with fulfilling the heating and cooling demands for ensuring occupants' thermal comfort. To mitigate such consumption, the use of insulation materials in building envelopes is widely recognized as an effective strategy to enhance a building's thermal inertia and improve its overall energy efficiency [2]. Traditional thermal insulation materials, such as mineral wool and polystyrene, are predominantly derived from non-renewable resources and contribute to considerable waste after disposal, resulting in a substantial environmental impact. In response to these challenges, bio-sourced materials (e.g., straw, wood and wool) are currently becoming popular in the construction industry due to their low carbon footprint and reduced environmental impact during their entire life cycle. Bio-sourced materials also offer favorable characteristics, including low density, low thermal conductivity [3,4] and good moisture-buffering capacity [5,6]. Their high porosity enables them to

absorb and store moisture within their pores and then release the moisture depending on prevailing climatic conditions. Incorporating bio-sourced materials into envelopes can achieve low-carbon buildings and contribute to the development of a smart built environment by regulating indoor microclimate.

Agricultural straw, e.g., wheat, rice and barley, is globally produced in billions of tons [7]. The management of straw presents a contentious issue due to prevalent practices of incineration and landfill. Straw bale constructions have been in practice for a long time due to the material's low density and low thermal conductivity. Straw composites, wherein straw fibers are bonded by alternative binders, including polyester fibers, synthetic resins, inorganic cementing materials and natural adhesives, are currently attracting considerable research efforts [8–11].

Many studies have investigated and assessed the thermal and hygric properties of straw composites. Ismail et al. [12] characterized the hygroscopic properties of wheat straw composites using standard tests and found the composites had high water vapor permeability due to their high open porosity. Javaid et al. [13] developed and characterized the thermal conductivity of rice straw composites using the guarded hot plate method, finding a low value of $0.023 \text{ W/(m}\cdot\text{K)}$, which was lower than that of traditional polystyrene. However, evaluations are commonly conducted at the material scale and under the steady-state condition, which is deemed insufficient to thoroughly assess the hygrothermal performance of straw composites as a building component because they are subjected to dynamic hygrothermal boundary conditions in actual service conditions [14,15]. Also, excessive moisture levels accumulating in the material due to prolonged exposure to dynamic environmental conditions can lead to issues of material and performance degradation.

To ensure the stability of indoor microclimate and promote energy saving, it is imperative to accurately examine the mechanisms of heat and moisture phenomenon and the hygrothermal performance of bio-sourced materials, such as straw composites, under more realistic conditions at large scales, such as the wall scale. Climate chambers provide a controlled boundary condition with less background noise than those in real-life scenarios. Slimani et al. [16] studied the hygrothermal behavior of a wood fiber insulation panel under a controlled environmental condition. Temperature and relative humidity measurements within the panel showed that the water vapor sorption was concomitant with the redistribution of liquid water. Latif et al. [17] compared the hygrothermal performance of three panels, i.e., a mineral wool panel, a wood fiber panel and a biond panel made of wood fiber and hemp-lime, by using a large climate chamber. The results showed that the wood fiber and biond panels, which were made of bio-sourced materials, had a higher thermal and hygric inertia than those of the mineral wool panel. Experimental analyses of the hygrothermal behavior of hemp concrete [18], date palm concrete [19] and straw concrete [20] at the wall scale under static and dynamic boundary conditions had been conducted. The results indicated that bio-sourced materials contribute to the mitigation of temperature and relative humidity variations and emphasized the substantial coupling effects between heat transfer and moisture transfer. However, the hygrothermal behavior of straw composites with natural binders that exhibit high insulating properties remains understudied. Due to straw composites' unique

microstructure and pore size distribution, the characteristics of heat transfer and moisture transfer of this material may differ significantly from those of other bio-based materials and straw concrete.

Hygrothermal models describing heat transfer and moisture transfer in porous media are commonly developed to simulate the thermal and hygric behaviors of bio-based walls under climatic conditions [21,22]. The main difference among various hygrothermal models is the driving potential of moisture migration, including relative humidity, moisture content, vapor pressure and capillary pressure. Kaoutari and Louahlia [23] developed a model of coupled heat-and-moisture transfer to describe the hygrothermal behavior in a dual-layered wall with a structural material and an insulating cob material. It was found that the insulating material, due to its higher absorption capacity, exhibited a more gradual change in moisture flux than the structural material. Mendes et al. [24] studied the moisture effects on conduction loads and found that neglecting the moisture transfer in the model led to an underestimation of annual heat flux by up to 59%, resulting in the underestimation of total energy consumption. Both vapor transport and liquid transport play a role in hygrothermal models to ensure accurate moisture behavior predictions through bio-based walls. However, in various studies, the models were often simplified to single-phase models by neglecting liquid transport [25,26]. Alioua, Agoudjil, Boudenne, et al. [27] compared numerical relative humidity (RH) profiles by using a Kunzel model with and without liquid transfer for date palm concrete subjected to step changes in relative humidity. The models exhibited deviations in RH values during the adsorption phase, with variations reaching 3.8%, 4% and 2.3% at depths of 3 cm, 7.5 cm and 12.5 cm, respectively. The liquid water transfer properties necessary for the models were estimated using the standard experimental characterization method of partial impregnation (ASTM C1794-15). However, standard measurements have certain limitations, such as susceptibility to human error and discontinuous testing. Moreover, liquid transport under dynamic conditions is difficult to accurately simulate, especially for highly hygroscopic materials, hence leading to notable discrepancies when compared with experimental data obtained from transient measurements. Therefore, dynamic and continuous measurement methods have been used to characterize the liquid water transfer coefficient.

The above literature highlights the high coupling between heat transfer and moisture transfer and the necessity of considering liquid water transfer for accurately modeling the hygrothermal behavior of bio-based materials at the wall scale. However, the hygrothermal behavior of straw composites with low density, low thermal conductivity and high moisture-buffering capacity remains underexplored. In addition, standard methods for characterizing liquid water transfer are limited in their ability to capture dynamic liquid transport, particularly for highly hygroscopic materials. To fill the gaps, the present study explored the hygrothermal behavior of a novel bio-based insulating wall made of a rice straw–alginate composite material. The hygrothermal performance of the novel straw composite wall was experimentally evaluated under various boundary conditions, which were isothermal, non-isothermal and dynamic conditions. An inverse analysis method was proposed to identify the liquid water transfer coefficient based on experimental measurements under the dynamic condition. Moreover, comparisons of the performances of the

transient heat transfer (TH) model, the coupled heat-and-moisture transfer (CHM) model and the coupled heat-and-moisture transfer with liquid water transport (CHMWL) model were conducted to provide insights into the coupling effects and the impacts of liquid transport on the hygrothermal behavior of the rice straw–alginate composite material.

2. Materials and methods

The overall framework of the study is depicted in **Figure 1**.

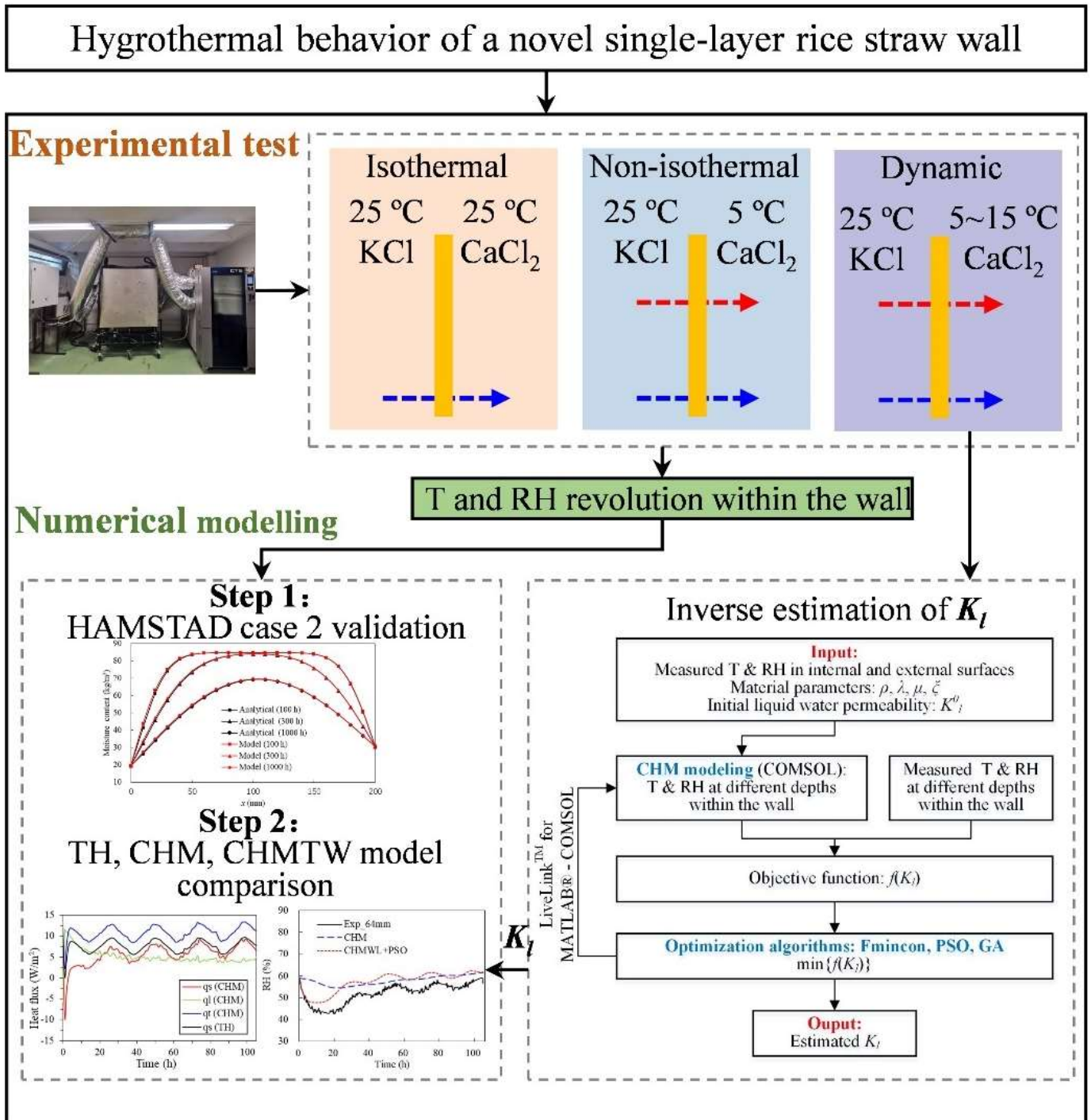


Figure 1. Overall framework of study.

2.1. Experimental method

2.1.1. Test wall and instrumentation

This study focused on a single-layer wall made entirely from a bio-sourced composite material, i.e., rice straw bonded using sodium alginate. This bio-based construction material has demonstrated excellent hygric and thermal performances, along with being a renewable and low-carbon material, making it suitable for sustainable development. A formulation of the rice straw with 8 wt% sodium alginate, developed using an external calcium crosslinking method, was selected due to its superior physical, thermal and hygric properties, which were previously determined in [28]. The test wall had a dimension of $50 \times 50 \times 8$ cm and was insulated from lateral surfaces using wood fiber insulation, vapor-resistance silicon and PVC films in order to guarantee a unidirectional heat transfer and moisture transfer through the thickness of the wall (see **Figure 2**).



Figure 2. (a) Hole network and (b) test wall.

The hygrothermal properties of the composite material have been characterized and summarized in **Table 1**. Specifically, the thermal conductivity of the material was measured in the dry state using the hot wire method. The thermal conductivity of the material is linearly dependent on its moisture content and the coefficient was set to 0.56 [29]. The sorption isotherm function was a Guggenheim-Anderson-de Boer fit of the mean values of adsorption and desorption isotherms. Water vapor permeability was assumed to be linearly related to relative humidity based on the results of dry cup and wet cup measurements.

Table 1. Hygrothermal properties of rice straw–alginate composite material.

Variable	Value/formula	Unit
Dry density	$\rho_m = 124$	kg/m ³
Mass specific heat capacity	$C_{p,m} = 1353$	J/kg/K
Thermal conductivity	$\lambda = 0.042 + 0.56 \frac{w}{1000}$	W/m/K
Sorption isotherm	$u = \frac{0.2978 \varphi}{(1 - 0.9560 \varphi)(1 - 0.9560 \varphi + 4.6027 \varphi)}$	kg/kg
Water vapor permeability	$\delta v = (6.69 \varphi + 1.44) \times 10^{-11}$	s

The wall was instrumented with five SHT75 sensors (Sensirion, Switzerland) to record temperature and relative humidity variations on both internal and external surfaces and at three different depths across the thickness of the test wall. The SHT75 sensor had a small size of $3.1 \times 5.1 \times 19.5$ mm, which was suitable for non-intrusive placement within the wall, thereby minimizing disruption to the surrounding environment. The accuracy values of temperature and relative humidity measurements were ± 0.5 °C and $\pm 2\%$, respectively. To facilitate sensor placement without compromising the wall's integrity, boreholes were carefully prepared and the resulting openings were sealed using silicone sealant (**Figure 2**). To reduce the disturbance of measurements, the sensors were inclined at 45° to the vertical plane.

2.1.2. Experimental facility

An experimental facility located at the CETHIL-INSA Lyon laboratory was designed for investigating the hygrothermal behavior of the building envelope component subjected to controlled boundary conditions [16,30]. The facility consists of two compartments, between which the test component was clamped. Compartment 1 was composed of an external stainless-steel compartment, a 60mm layer of polystyrene insulation, four heat exchangers connected to a cryothermostat and an internal stainless-steel compartment with a volume of 0.5 m^3 , hence offering an exchange surface of 1 m^2 from the external surface to the internal surface. Compartment 2 was composed of a 240mm multi-layer thin insulation, two 40mm layers of hemp wool insulation, an external stain-less compartment linked to a climate chamber with glass-wool-insulated ducts and an internal stain-less compartment with a volume of 0.5 m^3 from external to internal surfaces. The cryothermostat allowed for internal and external regulations based on the temperature measured by a PT100 sensor installed inside the cryothermostat and inside the compartment. This study utilized internal regulation to control the temperature in Compartment 1. Compartment 2 was connected to a climate chamber with a Clima Temperature System (CTS), which allowed for the generation of the desired temperature and relative humidity. The chamber contained a capacitive probe for measuring relative humidity and a PT100 probe for temperature measurement. In this experimental study, the relative humidity controller was not used in the CTS, and the desired relative humidity in Compartment 1 and Compartment 2 was achieved using a salt solution and a desiccant, respectively. Fans were installed at a height of 20 cm from the top of plastic boxes to homogenize the air conditions in compartments. A schematic diagram of the experimental setup is given in **Figure 3**. Thermo-hygro sensors were installed in the two compartments to continuously measure the hygrothermal loading applied to the test wall.

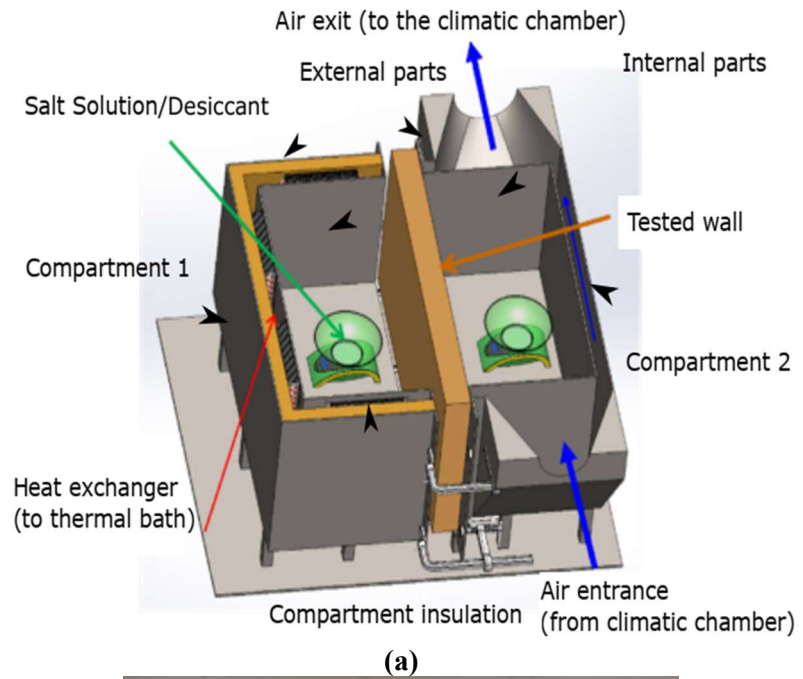


Figure 3. (a) Schematic diagram and (b) view of experimental setup at CETHIL-INSA Lyon laboratory.

2.1.3. Hygrothermal test conditions

Three tests, i.e., isothermal, non-isothermal and dynamic tests, were conducted in this study. Before each test, the test wall was preconditioned in room conditions until stabilization. For all the tests, the temperature in Compartment 1 was set to 25 °C and the relative humidity in Compartment 1 and Compartment 2 were regulated using a saturated salt solution, i.e., potassium chloride (KCl), and a desiccant, i.e., calcium chloride (CaCl₂), respectively. According to the ISO 12571 standard [31], the relative humidity values maintained by the saturated KCl solution and the CaCl₂ desiccant were approximately 85%RH and 40%RH. Water vapor was either absorbed or released until equilibrium was reached, stabilizing relative humidity. Furthermore, equilibrium relative humidity is largely independent of temperature fluctuations, making it an effective method for maintaining consistent

humidity [31].

For the isothermal test, Compartment 2 was maintained at a constant temperature of 25 °C for four days to eliminate temperature gradients. This test allowed for the investigation of the impact of moisture transfer and sorption on the thermal behavior of the test wall. For the non-isothermal test, Compartment 2 was kept at a constant temperature of 5 °C for two days. The temperature, relative humidity and vapor pressure gradient were in the same direction from the internal side to the external side. This test was performed to examine the influence of temperature gradient on the moisture transport of the test wall. The dynamic test involved temperature variations within Compartment 2 for four days. For a cycle of 24 h, the temperature was fluctuated between 5 °C and 15 °C with an amplitude of 10 °C. This test was conducted to investigate the hygrothermal behavior of the test wall under more realistic conditions.

Due to the uncertainty due to the boreholes, the actual depths of the sensors within the wall were measured by destroying the test wall after finishing all tests. The actual depths were 2.8 cm, 3.6 cm and 6.4 cm from the internal side to the external side of the wall.

2.2. CHM model

Heat transfer and moisture transfer models are developed based on mass and energy conservation. The bio-sourced materials are typically treated as porous media, consisting of air and water in both vapor and liquid forms. The key assumptions are as follows: (1) air transfer is not considered; (2) the solid phase is considered macroscopically homogeneous, isotropic and non-reactive; (3) local heat and moisture equilibrium are assumed within a material; (4) hysteresis phenomena between adsorption and desorption is neglected; (5) the moisture sorption capacity is assumed to be independent of temperature and (6) heat transfer and moisture transfer are treated as one-dimensional.

2.2.1. Mass transfer equilibrium equation

In porous materials, moisture transport is considered in two phases, which are water vapor and liquid water. According to the law of mass conservation, the moisture transport equation is given as [32]:

$$\rho_m \frac{\partial u}{\partial t} = -\nabla(g_v + g_l) \quad (1)$$

where ρ_m is the dry density, u (in kg/kg) is the mass moisture content, g_v (in kg/(m²·s·Pa)) is the water vapor transmission rate and g_l (in kg/(m²·s·Pa)) is the liquid water transmission rate.

In this model, water vapor transfer was described using Fick's law and the liquid water transfer was described using Darcy's law:

$$g_v = -\delta_p \frac{\partial P_v}{\partial x} \quad (2)$$

$$g_l = -K_l \frac{\partial P_c}{\partial x} \quad (3)$$

where δ_p (in kg/(m·s·Pa)) is the water vapor permeability, K_l (in kg/(m·s·Pa)) is the

liquid water permeability, P_v (in Pa) is the partial vapor pressure and P_c (in Pa) is the capillary pressure.

For convenience of calculations, this model adopted relative humidity as the driving factor for moisture transport. Therefore, the vapor pressure gradient can be deduced as:

$$\frac{\partial P_v}{\partial x} = \frac{\partial(\varphi P_{v,sat})}{\partial x} = \varphi \frac{dP_{v,sat}}{dT} \frac{\partial T}{\partial x} + P_{v,sat} \frac{\partial \varphi}{\partial x} \quad (4)$$

where $P_{v,sat}$ is the saturated water vapor pressure at the experimental temperature (in Pa) and φ is the relative humidity.

The temperature-dependent saturated water vapor pressure is described as [33]:

$$P_{v,sat}(T) = 610.5 \exp\left(\frac{17.269T}{237.3 + T}\right) \quad (5)$$

Based on the Kelvin equation, the capillary pressure gradient can be deduced as [34]:

$$\frac{\partial P_c}{\partial x} = \rho_l R_v \left(\ln(\varphi) \frac{\partial T}{\partial x} + \frac{T}{\varphi} \frac{\partial \varphi}{\partial x} \right) \quad (6)$$

where ρ_l (in kg/m³) is the liquid water density, R_v (in J/(kg·K)) is the water vapor gas constant and T (in K) is the thermodynamic temperature.

Therefore, substituting Eqs. (4) and (6) into Eq. (1), the moisture transfer equation is as follows:

$$\rho_m \xi \frac{\partial \varphi}{\partial x} = \frac{\partial}{\partial x} \left[\left(\delta_p \varphi \frac{dP_{v,sat}}{dT} + K_l R_v \ln(\varphi) \right) \frac{\partial T}{\partial x} + \left(\delta_p P_{v,sat} + K_l \rho_l R_v \frac{T}{\varphi} \right) \frac{\partial \varphi}{\partial x} \right] \quad (7)$$

where $\xi = \partial u / \partial \varphi$ represents the slope of sorption isotherm, while $u = f(\varphi)$.

2.2.2. Heat transfer equilibrium equation

Considering that the latent heat of vaporization is much higher compared with the sensible heat values of water vapor and liquid water, they were neglected in this model. The heat conservation in the material can be expressed by:

$$(\rho_m C_{p,m} + w C_{p,l}) \frac{\partial T}{\partial t} = \frac{\partial}{\partial x} \left(\lambda \frac{\partial T}{\partial x} \right) + L_v \left(\delta_p \left(\varphi \frac{\partial P_{v,sat}}{\partial x} \frac{\partial T}{\partial x} + P_{v,sat} \frac{\partial \varphi}{\partial x} \right) \right) \quad (8)$$

where λ (in W/(m·K)) is the thermal conductivity of the material, w (in kg/m³) is the moisture content, $C_{p,m}$ (in J/(kg·K)) is the mass specific heat capacity of the material, $C_{p,l}$ (in J/(kg·K)) is the mass specific heat capacity of water and L_v (in J/kg) is the latent heat of evaporation.

2.2.3. Boundary conditions

Before employing the CHM model for the test wall, it was verified on the HAMSTAD Benchmark Case 2. The boundary conditions of the internal and external sides are given as:

$$g_i = \beta_i (\varphi_i P_{sat,i} - \varphi_{surf,i} P_{sat,surf,i}) \quad (9)$$

$$g_e = \beta_e (\varphi_e P_{sat,e} - \varphi_{surf,e} P_{sat,surf,e}) \quad (10)$$

$$q_i = h_i(T_i - T) + L_v g_i \quad (11)$$

$$q_e = h_e(T_e - T) + L_v g_e \quad (12)$$

where g (in $\text{kg}/(\text{m}^2 \cdot \text{s})$) is the vapor flux at the boundaries, q (in W/m^2) is the heat flux at the boundaries, β (in $\text{kg}/(\text{m}^2 \cdot \text{s} \cdot \text{Pa})$) is the vapor transfer coefficient at the boundaries and h (in $\text{W}/(\text{m}^2 \cdot \text{K})$) is heat transfer coefficient at boundaries, ignoring radiation.

Considering that the convective heat and mass exchange coefficients were unknown, the surface temperature and relative humidity of the test wall in this study were measured and used as the boundary conditions, written as follows:

$$\varphi(x = 0, t) = \varphi_i(t) \quad (13)$$

$$\varphi(x = L, t) = \varphi_e(t) \quad (14)$$

$$T(x = 0, t) = T_i(t) \quad (15)$$

$$T(x = L, t) = T_e(t) \quad (16)$$

where L is the thickness of the test wall and t is the time step, while i and e indicate the internal and external surfaces of the test wall, respectively.

2.2.4. Solving methods

In this study, heat transfer and moisture transfer equations were modeled using the COMSOL Multiphysics software, a simulating environment that utilizes the finite element method. The COMSOL modeling tool has been extensively employed in hygrothermal studies [21,22,35]. The surface of the partial differential equation (PDE) module in COMSOL allows the incorporation of heat transfer and moisture transfer equations and establishes their coupling between them. In the module, the PDE is expressed in its general form as follows:

$$e_a \frac{\partial^2 u}{\partial t^2} + d_a \frac{\partial u}{\partial t} + \nabla \Gamma = f \quad (17)$$

where e_a is the mass coefficient, d_a is the damping coefficient, Γ is the conservative flux and f is the source term.

The dependent variable u is the temperature and relative humidity. According to the previous definition, the CHM model can be given as a matrix form:

$$\begin{bmatrix} \rho_m C_{p,m} + w C_{p,l} & 0 \\ 0 & \rho_m \xi \end{bmatrix} \begin{bmatrix} \frac{\partial T}{\partial t} \\ \frac{\partial \varphi}{\partial t} \end{bmatrix} = \nabla \left\{ \begin{bmatrix} \lambda + L_v \delta_p \varphi \frac{dP_{v,sat}}{dT} & \delta_p \varphi \frac{dP_{v,sat}}{dT} \\ \delta_p \varphi \frac{dP_{v,sat}}{dT} + K_l R_v \ln(\varphi) & \delta_p P_{v,sat} + K_l \rho_l R_v \frac{T}{\varphi} \end{bmatrix} \nabla \begin{bmatrix} T \\ \varphi \end{bmatrix} \right\} \quad (18)$$

2.2.5. Model validation

The HAMSTAD Benchmark Case 2 with a 200mm single-insulation layer wall was used to validate the numerical model. The temperature was always 20 °C in the hypothetical case. After initialized at a high relative humidity of 95%, the wall was exposed to boundary conditions at lower relative humidity. The internal and external relative humidity values were 65% and 45%, respectively. Additionally, the coefficients of the heat transfer and moisture transfer were assumed as 25 $\text{W}/(\text{m}^2 \cdot \text{K})$

and 1.0×10^{-3} s/m, respectively. **Table 2** presents the material properties. Due to the zero gradient of temperature, the moisture content profiles in the wall can be solved analytically, providing exact solutions without the need for numerical approximations. The simulation lasted 1000 h and the obtained results were moisture profiles at 100 h, 300 h and 1000 h.

Table 2. Hygrothermal properties of material in HAMSTAD Benchmark Case 2.

Material property	Value/formula	Unit
Density, ρ_m (kg/m ³)	$\rho_m = 525$	kg/m ³
Thermal conductivity, λ (W/(m·K))	$\lambda = 0.15$	W/(m·K)
Specific heat capacity, $C_{p,m}$ (J/(kg·K))	$C_{p,m} = 800$	J/(kg·K)
Sorption isotherm, w (kg/m ³)	$w = \frac{116}{\left(1 - \frac{1}{0.118} \ln \varphi\right)^{0.869}}$	kg/m ³
Water vapor permeability, δ_v (kg/(m·s·Pa))	$\delta_v = 1 \times 10^{-15}$	kg/(m·s·Pa)
Moisture diffusivity, D_w (m ² /s)	$D_w = 6 \times 10^{-10}$	m ² /s

It can be observed from **Figure 4** that the simulated results produced by the CHM model show a good agreement with analytical solutions [36]. The maximum relative errors between the results of the CHM model and analytical solutions were 5.4%, 4.3% and 2.9% at 100 h, 300 h and 1000 h, respectively. These results demonstrated the effectiveness of the CHM.

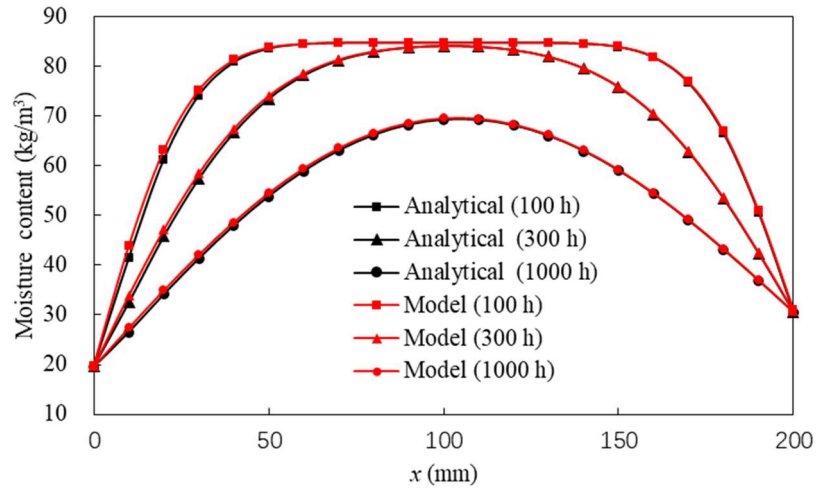


Figure 4. Moisture content profiles for HAMSTAD Benchmark Case 2.

2.3. Liquid water permeability determination

The standard method of measuring liquid water transfer coefficients has certain limitations, including susceptibility to human error and discontinuous testing. Also, it is difficult to accurately simulate liquid transport under a dynamic condition, especially for highly hygroscopic materials, hence leading to notable discrepancies when compared with experimental data obtained from transient measurements. Therefore, in this study, an inverse parameter estimation method was proposed to identify liquid water permeability based on the dynamic test at the wall scale.

2.3.1. Inverse analysis

In this study, liquid water permeability, K_l , was regarded as an unknown property to be identified from temperature and relative humidity measurements at the three depths within the wall under the dynamic condition. The framework of the inverse identification of K_l is illustrated in **Figure 5**.

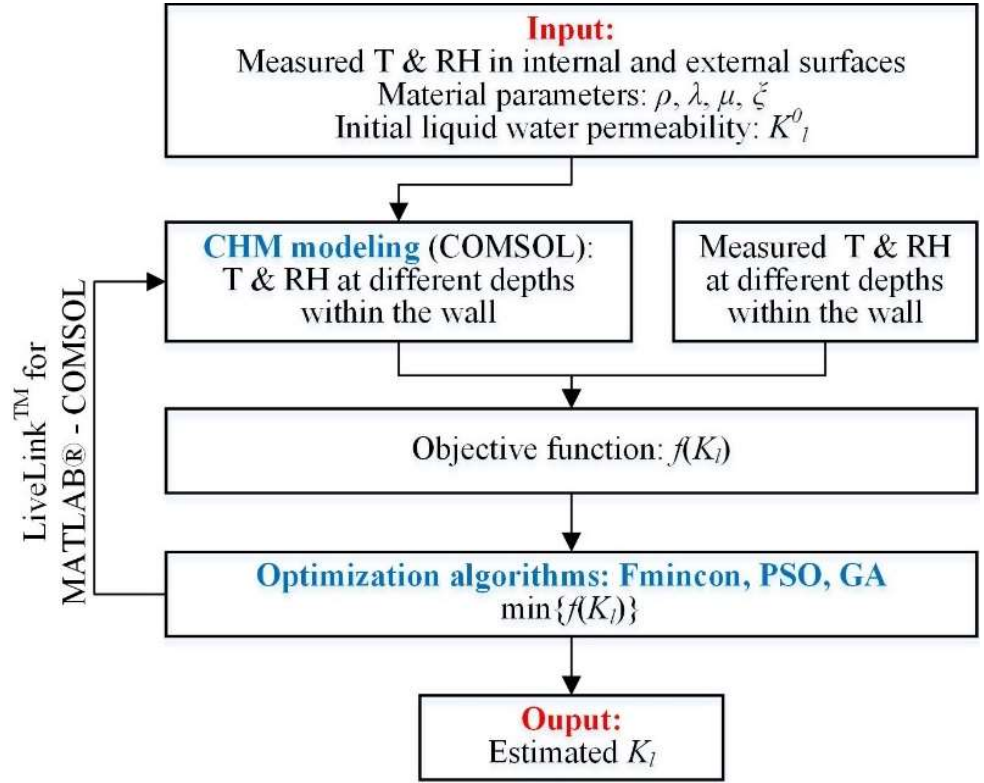


Figure 5. Parameter estimation workflow.

Note that K_l has a very wide range. According to [37], the K_l of a medium-density fiberboard ranges from 0 to 1.17×10^{-16} . For simplicity, K_l was assumed as a linear function of moisture content, which is as follows:

$$K_l = (a \times w) \times 10^{-17} \quad (19)$$

where w (in kg/m^3) represents the moisture content in the material and a represents the dimensionless parameter to be estimated, with the range from 0 to 100.

For evaluating different solutions, this study defined a multi-objective function as the sum of the squared error between the results of the measurements (including temperature and relative humidity) and the simulations by the CHM model:

$$f(a) = \sum_{n=1}^N \sum_{l=1}^L \left(\frac{y_{nl} - y_{nl}(a)}{\sigma_n} \right)^2 \quad (20)$$

where y_{nl} represents l data points for each measured variable n (temperature and relative humidity), while $y_{nl}(a)$ represents the variable calculated from the direct CHM model inputting the estimated K_l .

Therefore, the expected parameter for K_l can be obtained by minimizing the objective function as follows:

$$\min f(a) = \sum_{n=1}^N \sum_{l=1}^L \left(\frac{y_{nl} - y_{nl}(\theta)}{\sigma_n} \right)^2 \quad (21)$$

2.3.2. Optimization algorithms

Fmincon is a kind of sequential quadratic programming algorithm in the MATLAB optimization toolbox for solving the quadratic programming subproblem at each iteration. It is a popular local search method, which finds the constrained minimum of a scalar nonlinear function. This is in contrast to the commonly used Levenberg-Marquart algorithm, which minimizes a sum of squares. Thus, Fmincon was selected instead of the Levenberg-Marquart algorithm because of its ability to include boundary constraints. In this study, the interior point algorithm was selected in Fmincon, using adjoint sensitivities for evaluating the gradient of the target function. In this study, the maximum iteration was set to 10.

The Particle Swarm Optimization (PSO) algorithm is a stochastic search method inspired by the unique social behavior of some natural creatures, such as the collective movement of bird flocks and fish schools [38]. In this algorithm, particles are described by their positions and velocities. The movement of the particles can be affected by their memory, as well as the best particles found by all the particles. In this way, all the particles can share the knowledge of reasonable solutions.

The PSO algorithm has few hyperparameters and fast convergence. The velocity vector and the position vector of each particle i in the PSO algorithm are denoted by $V_i = [v_{i1}, v_{i2}, \dots, v_{iN}]$ and $X_i = [X_{i1}, X_{i2}, \dots, X_{iN}]$, respectively. Particle i will update its velocity and position from the influence of the previous best position of particle i , i.e., $pbest_i = [p_{i1}, p_{i2}, \dots, p_{iN}]$, and the best one in the whole population, i.e., $gbest = [g_1, g_2, \dots, g_N]$. Vectors V_i and X_i are firstly stochastically initialized and are updated according to equations as follows:

$$V_i^{k+1} = \omega \cdot V_i^k + c_1 \cdot rand_1 \cdot (pbest_i - X_i^k) + c_2 \cdot rand_2 \cdot (gbest - X_i^k) \quad (22)$$

$$X_i^{k+1} = X_i^k + V_i^{k+1} \quad (23)$$

where ω is the inertia factor, c_1 is the personal learning coefficient and c_2 is the global learning coefficient, where c_1 and c_2 are set equal generally in this study to balance the effect of random factors, while $rand_1$ and $rand_2$ are random numbers between 0 and 1. In this study, the particle size and generation size were set to 10.

The Genetic Algorithm (GA) is a stochastic global search approach activated by the evolution mechanism [39]. Compared with the other two algorithms, the GA scarcely falls into the local optima despite of discontinuity, irregularity and noise of the defined objective function. The GA first initializes a population, i.e., a set of individuals, which is randomly generated. For each generation, the individuals are sorted and selected by evaluating the objective function. Then, new individuals are generated based on the selection, crossover and mutation. In this study, the population size and generation size were set to 10.

2.3.3. Performance assessment metrics

For evaluating the modeling performance using the estimated K_l found by different optimization algorithms, this study employed two metrics, which were the

mean absolute error (MAE) and the root mean squared error (RMSE) [40]:

$$MAE = \frac{\sum_{t=1}^N |\tilde{y}_t - y_t|}{N} \quad (24)$$

$$RMSE = \sqrt{\frac{\sum_{t=1}^N (\tilde{y}_t - y_t)^2}{N}} \quad (25)$$

where y_t is the measured temperature or relative humidity at different depths, \tilde{y}_t is the simulated temperature or relative humidity at different depths, t is the timestep and N is the maximum timestep.

3. Results and discussion

3.1. Experimental analysis

Figure 6 shows the temperature, relative humidity and calculated partial vapor pressure under the isothermal condition. As can be seen, the internal air relative humidity stabilized at 81% and the external air relative humidity firstly decreased rapidly and then increased to a nearly constant value of 39%. The partial vapor pressure gradient from the internal side to the external side as determined by Equation (26) was about 13.6 hPa.

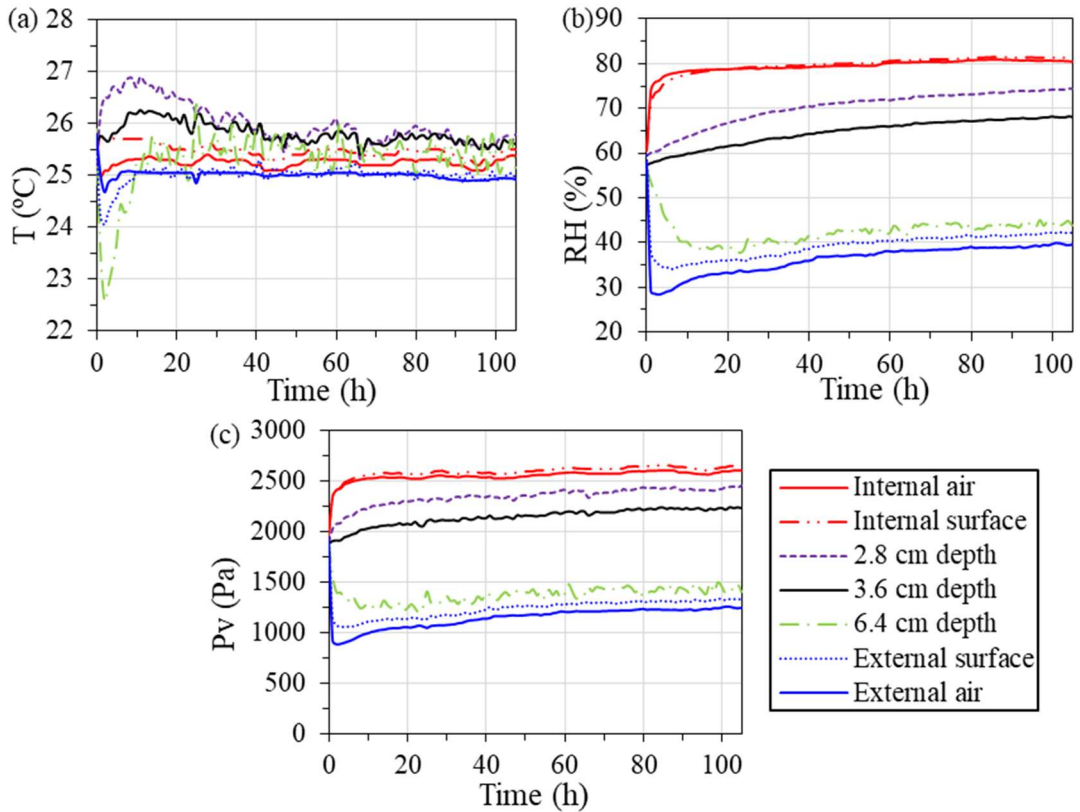


Figure 6. Evolution in time at depths of 2.8 cm, 3.6 cm and 6.4 cm on internal side under isothermal condition: (a) temperature, (b) relative humidity and (c) partial vapor pressure.

$$P_v = RH/100 \times \text{Exp}\left(\frac{17.26 \times T}{237.5 + T}\right) \quad (26)$$

Upon the sudden increase in internal air relative humidity and decrease in external air relative humidity, temperature variations were obvious at specific depths within the test wall. Notably, at $x = 2.8$ cm and $x = 3.6$ cm, increases in temperature of approximately 1.4 °C and 0.7 °C occurred, respectively. Conversely, a sharp decrease of about 3.2 °C was observed at $x = 6.4$ cm. The exothermic phenomenon was a consequence of the increase in internal partial vapor pressure, leading to more moisture absorbed by the material. Conversely, the endothermic phenomenon was from the decrease in external partial vapor pressure, prompting the evaporation of liquid water accompanied by heat absorption, leading to the cooling effect on the material. Furthermore, the temperature values at $x = 2.8$ cm and $x = 3.6$ cm slightly exceeded both the internal ambient air temperature and external ambient air temperature instead of maintaining between them. This was attributed to water vapor condensation occurring within the wall. These results demonstrated the significant influence of moisture transfer on heat transfer dynamics within the test wall.

Figure 7 shows the temperature, relative humidity and calculated partial vapor pressure under the non-isothermal condition. The internal air relative humidity stabilized at 75% and the external air relative humidity firstly decreased rapidly and then gradually increased to a nearly constant value of 53%. The temperature stabilized more quickly than the relative humidity in both compartments. The internal and external air temperature values were 24 °C and 7 °C, respectively, resulting in a temperature gradient of 17 °C. The vapor pressure gradient was 17 hPa. The direction of heat flow and vapor flow was from the internal side to the external side.

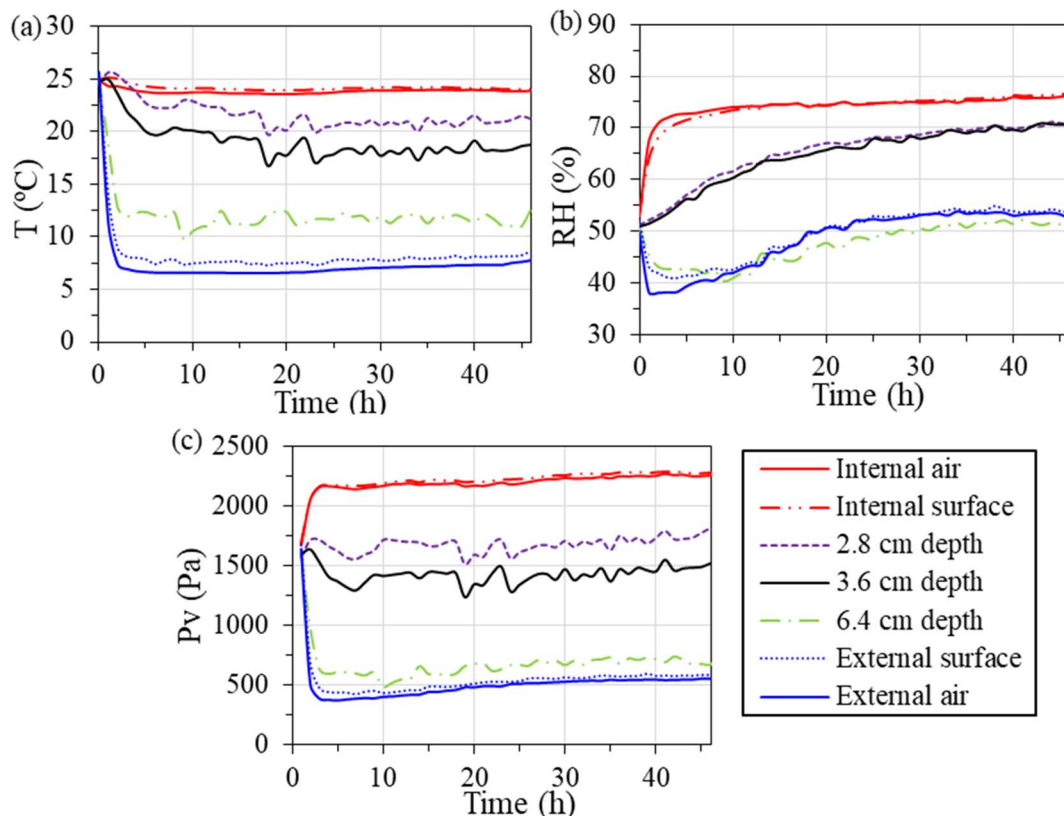


Figure 7. Evolution in time at depths of 2.8 cm, 3.6 cm and 6.4 cm on internal side under non-isothermal condition: (a) temperature, (b) relative humidity and (c) partial vapor pressure.

The relative humidity values at $x = 2.8$ cm and $x = 3.6$ cm exhibited remarkable similarity due to the higher saturation vapor pressure at $x = 2.8$ cm offsetting the effect of partial water vapor pressure. The partial vapor pressure distributions within the test wall under the isothermal and non-isothermal conditions were compared, as shown in **Figure 8**. It can be seen that the non-isothermal test yielded a significantly larger partial vapor pressure difference between the internal surface and $x = 2.8$ cm compared with that of the isothermal test. A possible explanation for this is that the enhanced moisture sorption resulting from the lower temperature under the non-isothermal condition led to increased water vapor condensation and the subsequent reduced partial vapor pressure. These results demonstrated the high coupling effects of heat transfer and moisture transfer processes and that the same direction of heat flow and moisture flow facilitated moisture redistribution within the test wall. It should be noted that the relative humidity gradient was smaller due to the influence of temperature.

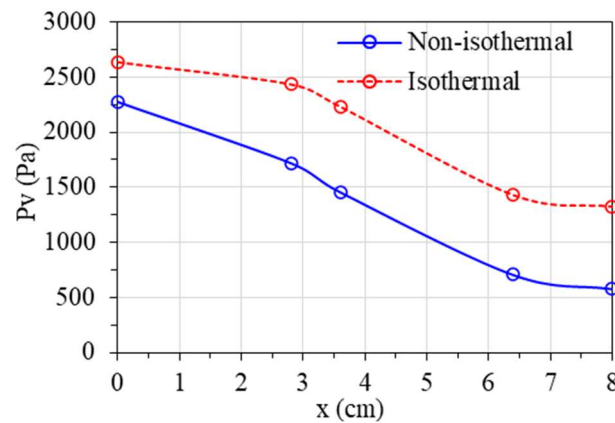


Figure 8. Partial vapor pressure distributions under isothermal and non-isothermal conditions after stabilization.

Figure 9 shows the temperature, relative humidity and calculated partial vapor pressure evolution under the dynamic condition. The temperature variation at the internal surface closely followed that of the external surface but with a thermal phase shift. A thermal phase shift is a commonly used parameter to assess the effectiveness of a material in providing indoor thermal comfort. It is defined as the time required for the propagation of external temperature oscillations from the exterior surface to the interior surface of the material [41]. A material with a high thermal phase shift contributes to a comfortable indoor environment.

The thermal phase shift provided by the 8cm rice straw–alginate wall panel with a density of 124 kg/m^3 was about 2.5 h, which was comparable to that of wood fiber insulation, where the thermal phase shift is 1.75 h for a density of 160 kg/m^3 and a thickness of 6 cm, and 3 h for a density of 150 kg/m^3 and a thickness of 8 cm [42]. This result demonstrated that the material is effective in providing indoor thermal comfort.

The partial vapor pressure within the wall was a reliable indicator of its water content and was significantly influenced by the thermal cycle. It can be seen from **Figure 9** that the partial vapor pressure at all three depths closely followed the corresponding temperature variations, i.e., an increase during heating phases and a

decrease during cooling periods. However, at $x = 2.8$ cm and $x = 3.6$ cm, the relative humidity remained relatively stable after initial increases. These results led to the assumption that temperature strongly affects the hygric behavior of a porous material, further indicating the effect of temperature on the moisture sorption capacity curve. The stability of relative humidity at the two depths can be explained by the combined effect of temperature-dependent saturation vapor pressure and the moisture sorption capacity of the material. Specifically, with an increase in temperature, the moisture sorption capacity of the material diminished, leading to an increased water vapor evaporation rate and consequently a rise in relative humidity. However, the increase in temperature also influenced the saturation vapor pressure, which contributed to a reduction in relative humidity. The relationships between temperature, moisture sorption capacity and water vapor saturation played an important role in governing the stability of relative humidity within the wall.

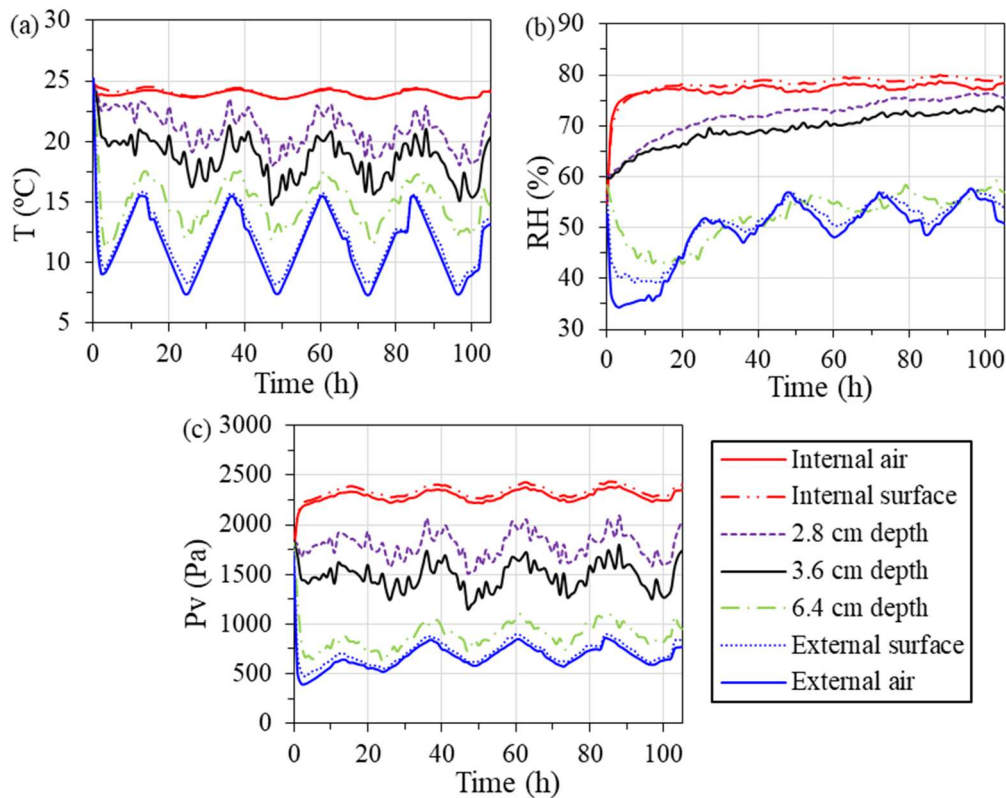


Figure 9. Evolution in time at depths of 2.8 cm, 3.6 cm and 6.4 cm on internal side under dynamic condition: (a) temperature (b) relative humidity and (c) partial vapor pressure.

3.2. Numerical analysis

Figure 10 presents a comparison of the experimental results and the numerical results obtained by the CHM model and TH model at the three depths within the test wall under all three conditions. As can be seen, the temperature variations at the three depths were more accurately predicted by the CHM model than by the TH model under all three conditions, indicating that moisture transport should be considered for modeling the thermal behavior of this material. For example, under the dynamic condition, the TH model exhibited maximum errors of 3.5 °C, 3.0 °C and 1.9 °C at depths of 2.8 cm, 3.6 cm and 6.4 cm, respectively, while the CHM

model achieved errors of 2.9 °C, 1.4 °C and 1.4 °C, respectively. **Figure 11** shows the sensible heat flux, latent heat flux and total heat flux on the interior surface as predicted by the CHM model, along with the sensible heat flux as predicted by the TH model, under the dynamic condition. The sensible heat flux periodically fluctuated with T . From the inter-model comparison, the TH model overestimated the sensible heat flux by 11.3% compared with that of the CHM model. Moreover, the latent heat flux accounted for 37.7% of the total heat flux predicted by the CHM model. Consequently, the TH model underestimated the total heat flux by 30.6% in comparison with that of the CHM model. Such discrepancies can potentially lead to an underestimation of a cooling load transmitted through a wall during building energy simulations.

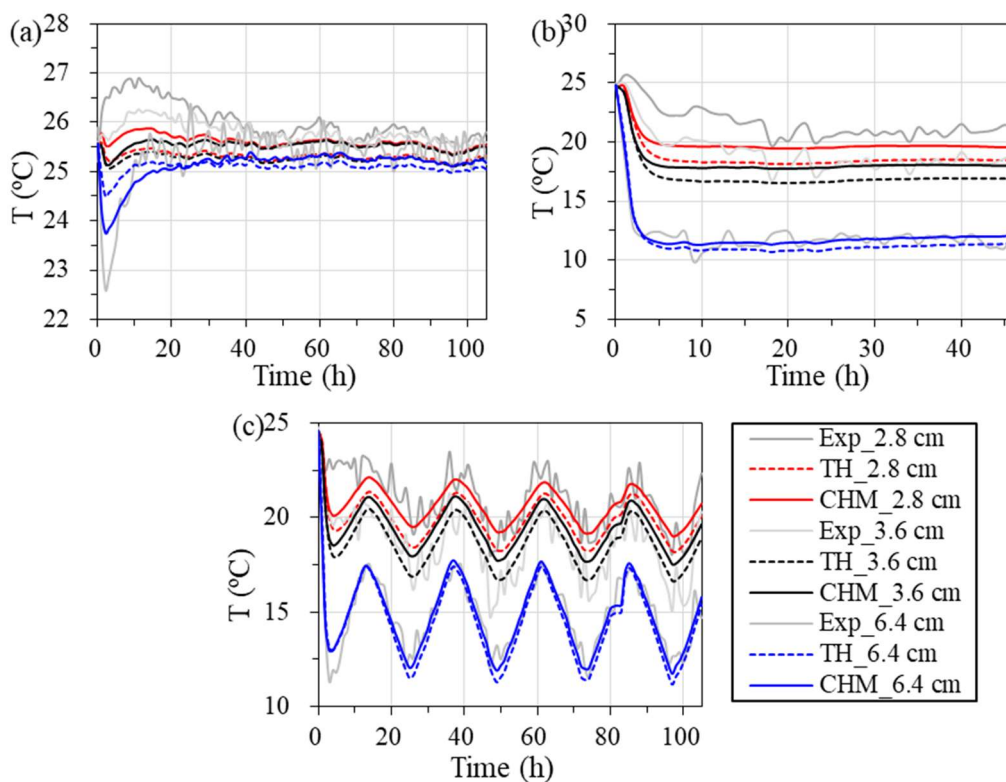


Figure 10. Temperature evolution within wall predicted by CHM and TH models: (a) isothermal test (b) non-isothermal test and (c) dynamic test.

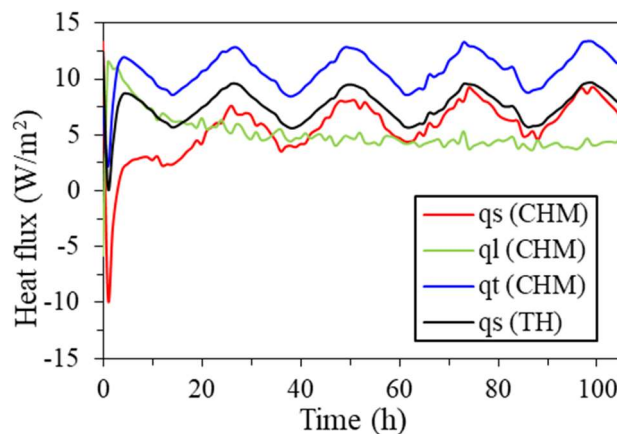


Figure 11. Heat fluxes through interior surface predicted by CHM and TH models.

Despite achieving improved results compared with those of the TH model, the CHM model still exhibited discrepancies in predicting partial vapor pressure and temperature at $x = 2.8$ cm and $x = 3.6$ cm with slightly lower values and $x = 6.4$ cm with slightly higher values than those of experimental measurements. This indicates that the actual response of the wall was faster than the numerical results, which can be attributed to several factors, including the heterogenization of the initial conditions across the thickness of the wall and certain simplifications made in the CHM model. One prominent factor contributing to the discrepancies is the ignoring of liquid water transport and the hysteresis effect of moisture sorption in the CHM model, which added the difficulty in capturing the hygrothermal behavior of particularly of a bio-sourced material characterized by its high moisture buffering capacity. Further studies in modeling moisture transport and sorption phenomena are needed to enhance the fidelity of numerical simulations and better understand the hygrothermal performance of bio-sourced materials under varying environmental conditions.

3.3. Comparison of models with and without liquid transfer

Table 3 shows liquid water permeability (K_l) as determined by the different optimization algorithms, i.e., Fmincon, PSO and GA. As can be seen, similar values of K_l were obtained by the three optimization algorithms. To assess the effectiveness of the estimated K_l , the simulation results using these K_l values were compared with the results of the CHM model, ignoring liquid transfer.

Table 3. Liquid water permeability determined by different optimization algorithms.

Optimization algorithm	Liquid water permeability, K_l (kg/(m·s·Pa))
Fmincon	3.4441×10^{-16}
PSO	3.4071×10^{-16}
GA	3.7176×10^{-16}

In **Table 4**, the errors of temperature and relative humidity predicted by the CHM model and the CHMWL model are summarized. Consistent with the previous results, there were negligible effects on K_l as determined by the different optimization algorithms on temperature and relative humidity predictions. Also, compared with the CHM model, which ignored liquid water transfer, the CHMWL model with the three algorithms, taking liquid transport into account, highly reduced the errors in predicting relative humidity at all depths. According to the MAE metric, the CHMWL model decreased the error by 61%, 57% and 8% at depths of 28 mm, 36 mm and 64 mm, respectively, compared with those predicted by the CHM model. The minor improvement at the depth of 64 mm was attributed to low relative humidity. At this depth, moisture transport was mainly driven by vapor pressure accompanied by a very small capillary pressure. And thus, by applying the linear function as moisture content, liquid water transfer could be overestimated, leading to errors in the prediction of relative humidity. Among the models, the difference in temperature error was actually not significant.

Table 4. Performance comparison between numerical models with and without liquid water transfer under dynamic condition.

Parameter	Model	$x = 28 \text{ mm}$		$x = 36 \text{ mm}$		$x = 64 \text{ mm}$	
		MAE	RMSE	MAE	RMSE	MAE	RMSE
T (°C)	CHM	0.79	1.03	1.07	1.31	0.46	0.58
	CHMWL + Fmincon	0.83	1.08	0.99	1.22	0.51	0.66
	CHMWL + PSO	0.83	1.08	0.99	1.22	0.51	0.66
	CHMWL + GA	0.83	1.08	0.99	1.22	0.51	0.66
RH (%)	CHM	5.6	5.8	4.9	5.1	5.9	6.7
	CHMWL + Fmincon	2.3	2.4	2.1	2.4	5.4	5.8
	CHMWL + PSO	2.2	2.4	2.1	2.3	5.4	5.8
	CHMWL + GA	2.2	2.4	2.1	2.3	5.4	5.8

Note: CHMWL + Fmincon, CHMWL + PSO and CHMWL + GA denote models with liquid water permeability determined using Fmincon, PSO and GA optimization algorithms, respectively.

For a more intuitive comparison, **Figure 12** illustrates the relative humidity variations at different depths predicted by the CHM model and the CHMWL + PSO model, together with the measurements. As can be seen, compared with the CHM model, the CHMWL + PSO model predicted a relative humidity curve that is closer to the experimental curve for depths of 28 mm and 36 mm. Additionally, at the depth of 64 mm, despite the higher relative humidity predicted by the CHMWL + PSO model, this model could track the periodic fluctuations. Therefore, it can be concluded that the inversely determined liquid water permeability contributed to numerical calculations.

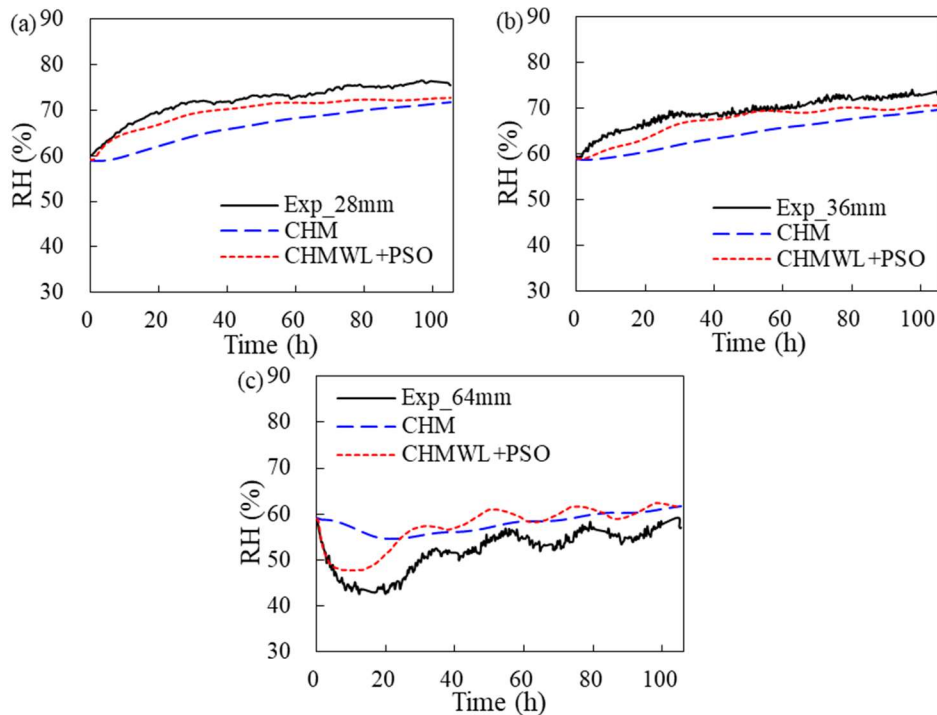
**Figure 12.** Comparison of relative humidity predicted by CHM and CHMWL + PSO models under dynamic condition at depths of (a) 28 mm, (b) 36 mm and (c) 64 mm.

Figure 13 shows the sensible heat flux (q_s) through the interior surface predicted by the CHM and CHMWL + PSO models. A small discrepancy in the sensible heat flux can be observed between these two models, which is consistent with the result of the temperature simulation. **Figure 14** shows the vapor flux, liquid water flux and total moisture flux of the interior surface predicted by the CHMWL + PSO model and the vapor flux predicted by the CHM model. It is seen that the moisture flux predicted by the CHWL + PSO model was much higher than that predicted by the CHM model.

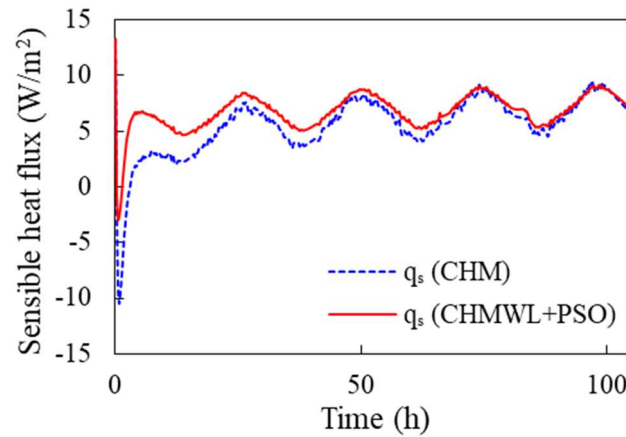


Figure 13. Sensible heat flux (q_s) through interior surface predicted by CHM model and CHMWL + PSO model.

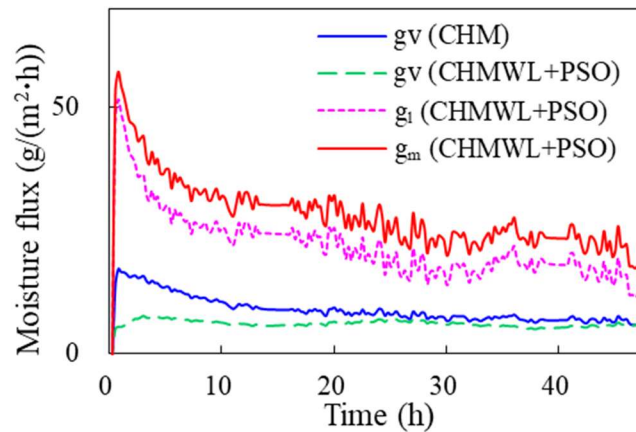


Figure 14. Moisture fluxes through interior surface predicted by CHM model and CHMWL + PSO model.

The identified K_l was further validated via another experiment, where the wall was subjected to a non-isothermal condition in order to test the robustness of the K_l . **Table 5** and **Figure 15** show the results of temperature and relative humidity simulated by the CHM and CHMWL + PSO models. These results are consistent with the previous results. From **Figure 15**, at depths of 28 mm and 36 mm, the simulated curves of relative humidity by the CHMWL + PSO model were closer to the experimental curves compared with those simulated by the CHM model, especially in the transient state. This is useful information because an unsteady process usually exists, as building envelopes are normally exposed to fluctuating conditions in a real-world environment. Therefore, the K_l determined under the

dynamic condition can be used to reproduce the transport of liquid water in such a wall when exposed to different boundary conditions. Nevertheless, the assumption of K_l as a linear function of moisture content makes it difficult to completely describe the transport of liquid water across the thickness of the wall when exposed to different boundary conditions. In future studies, appropriate functions for liquid water permeability should be chosen to simulate the realistic moisture behavior of the material.

Table 5. Performance comparison between numerical models with and without liquid water transfer under non-isothermal condition.

Parameter	Model	$x = 28 \text{ mm}$		$x = 36 \text{ mm}$		$x = 64 \text{ mm}$	
		MAE	RMSE	MAE	RMSE	MAE	RMSE
T (°C)	CHM	1.69	1.97	1.03	1.38	0.50	0.62
	CHMWL + PSO	1.99	2.21	1.13	1.43	0.52	0.65
RH (%)	CHM	8.1	8.4	9.4	9.9	3.8	4.8
	CHMWL + PSO	0.9	1.0	2.4	2.5	6.6	6.8

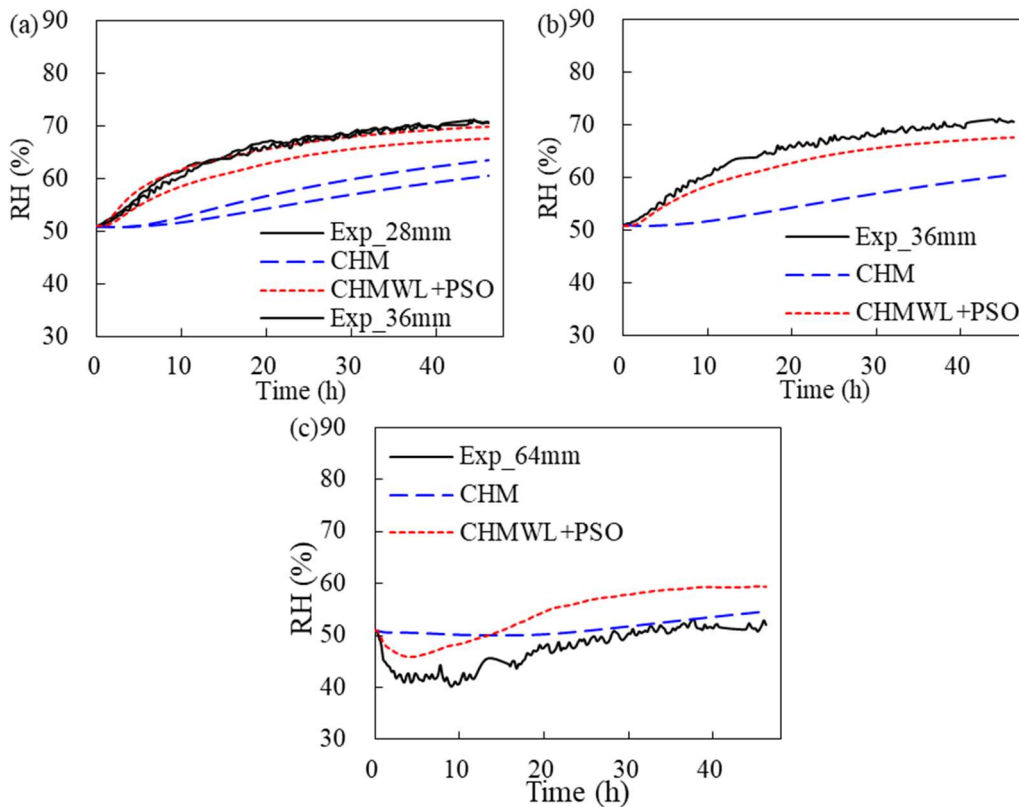


Figure 15. Comparison of relative humidity predicted by CHM and CHMWL + PSO transfer models under non-isothermal condition at depths of (a) 28 mm, (b) 36 mm and (c) 64 mm.

4. Conclusions and future works

This study focused on the analysis of the hygrothermal behavior of a novel bio-based material made from rice straw and sodium alginate. Both experimental and numerical investigations were conducted on the rice straw–alginate wall under various conditions, which were isothermal, non-isothermal, and dynamic

environments. The performance of the CHM model was compared with that of the TH model. Liquid water permeability was estimated using the inverse method, and the effects of liquid water transport on the hygrothermal behavior were examined. The main conclusions are as follows:

- (1) A high coupling effect of heat transfer and moisture transfer processes and the same direction of heat flow and moisture flow facilitated moisture redistribution within the test wall. The thermal phase shift provided by the material was about 2.5 h, which was comparable to that of wood fiber insulation.
- (2) A pure conduction model was insufficient to simulate and predict temperature variations and thermal load through the wall. For example, the TH model underestimated the total heat flux up to 30.6% compared with that of the CHM model.
- (3) Liquid water transport was essential for modeling moisture transfer through the wall. The CHMWL model decreased the MAE by 61%, 57% and 8% at the three depths of 28 mm, 36 mm and 64 mm from the interior to the exterior, respectively, compared with those of the CHM model.

This study was limited to a single-layer bio-based wall and specific environmental conditions. Future works should expand to multilayer wall systems, which are more representative of real-world applications. Additionally, a comparison with traditional wall systems, such as those using EPS and wood fiber insulation, should be conducted to provide a more comprehensive assessment of the hygrothermal performance and practical potential of bio-based walls in the construction industry.

Author contributions: Conceptualization, YZ; methodology, YZ and AT; validation, YZ and AT; writing—original draft preparation, YZ and LX; writing—review and editing, YZ and AT; supervision, AT and MEM; funding acquisition, YZ and MEM. All authors have read and agreed to the published version of the manuscript.

Funding: The authors would like to thank the Région Auvergne-Rhône-Alpes for its financial contributions. In addition, the authors would like to thank the China Scholarship Council for providing financial support for the study in France.

Conflict of interest: The authors declare no conflict of interest.

Nomenclature

C_p	Specific heat capacity (J/(kg·K))	ρ	Density (kg/m ³)
D_w	Moisture diffusivity (m ² /s)	λ	Thermal conductivity (W/(m·K))
g_v	Water vapor transmission rate (kg/(m ² ·s·Pa))	φ	Relative humidity (-)
g_l	Liquid water transmission rate (kg/(m ² ·s·Pa))	δ_p	Water vapor permeability (kg/(m·s·Pa))
g_i	Vapor flux at inner surface (kg/(m ² ·s))	ζ	Slope of sorption isotherm
g_e	Vapor flux at outer surface (kg/(m ² ·s))	β	Liquid fraction
K_l	Liquid water permeability (kg/(s·Pa))		
L_v	Latent heat of evaporation (J/kg)	TH	Thermal heat transfer
P_c	Capillary pressure (Pa)	CHM	Coupled heat-and-moisture transfer

P_v	Partial vapor pressure (Pa)	CHMWL	Coupled heat-and-moisture transfer with liquid water transport
$P_{v,sat}$	Saturated vapor pressure (Pa)		
q_i	Heat flux at inner surface (W/m^2)		
q_e	Heat flux at outer surface (W/m^2)		
R_v	Water vapor gas constant ($J/(kg \cdot K)$)		
T	Temperature ($^{\circ}C$)		
u	Mass moisture content (kg/kg)		
w	Volumetric moisture content (kg/m^3)		

References

- Chen Y, Thomas Ng S. Factoring in embodied GHG emissions when assessing the environmental performance of building. *Sustainable Cities and Society*. 2016; 27: 244–252. doi: 10.1016/j.scs.2016.03.015
- Ramlee NA, Naveen J, Jawaid M. Potential of oil palm empty fruit bunch (OPEFB) and sugarcane bagasse fibers for thermal insulation application – A review. *Construction and Building Materials*. 2021; 271: 121519. doi: 10.1016/j.conbuildmat.2020.121519
- Muthuraj R, Lacoste C, Lacroix P, et al. Sustainable thermal insulation biocomposites from rice husk, wheat husk, wood fibers and textile waste fibers: Elaboration and performances evaluation. *Industrial Crops and Products*. 2019; 135: 238–245. doi: 10.1016/j.indcrop.2019.04.053
- Mati-Baouche N, De Baynast H, Lebert A, et al. Mechanical, thermal and acoustical characterizations of an insulating bio-based composite made from sunflower stalks particles and chitosan. *Industrial Crops and Products*. 2014; 58: 244–250. doi: 10.1016/j.indcrop.2014.04.022
- Nguyen DM, Grillet AC, Bui QB, et al. Building bio-insulation materials based on bamboo powder and bio-binders. *Construction and Building Materials*. 2018; 186: 686–698. doi: 10.1016/j.conbuildmat.2018.07.153
- Viel M, Collet F, Lanos C. Development and characterization of thermal insulation materials from renewable resources. *Construction and Building Materials*. 2019; 214: 685–697. doi: 10.1016/j.conbuildmat.2019.04.139
- Hassan SS, Williams GA, Jaiswal AK. Emerging technologies for the pretreatment of lignocellulosic biomass. *Bioresource Technology*. 2018; 262: 310–318. doi: 10.1016/j.biortech.2018.04.099
- Liuzzi S, Rubino C, Martellotta F, et al. Characterization of biomass-based materials for building applications: The case of straw and olive tree waste. *Industrial Crops and Products*. 2020; 147: 112229. doi: 10.1016/j.indcrop.2020.112229
- Dušek J, Jerman M, Podlena M, et al. Sustainable composite material based on surface-modified rape straw and environment-friendly adhesive. *Construction and Building Materials*. 2021; 300: 124036. doi: 10.1016/j.conbuildmat.2021.124036
- Rojas C, Cea M, Iriarte A, et al. Thermal insulation materials based on agricultural residual wheat straw and corn husk biomass, for application in sustainable buildings. *Sustainable Materials and Technologies*. 2019; 20: e00102. doi: 10.1016/j.susmat.2019.e00102
- Romano A, Bras A, Grammatikos S, et al. Dynamic behaviour of bio-based and recycled materials for indoor environmental comfort. *Construction and Building Materials*. 2019; 211: 730–743. doi: 10.1016/j.conbuildmat.2019.02.126
- Ismail B, Belayachi N, Hoxha D. Hygric properties of wheat straw biocomposite containing natural additives intended for thermal insulation of buildings. *Construction and Building Materials*. 2022; 317: 126049. doi: 10.1016/j.conbuildmat.2021.126049
- Javaid A, Jain D, Kwatra N. Pre-treatment and its effect on the thermal conductivity of natural lignocellulosic rice straw stubble waste boards: Analysis vis a vis potential for the civil engineering applications. *Construction and Building Materials*. 2024; 445: 137903. doi: 10.1016/j.conbuildmat.2024.137903
- Thomson A, Walker P. Durability characteristics of straw bales in building envelopes. *Construction and Building Materials*. 2014; 68: 135–141. doi: 10.1016/j.conbuildmat.2014.06.041
- Laborel-Préneron A, Ouédraogo K, Simons A, et al. Laboratory test to assess sensitivity of bio-based earth materials to fungal growth. *Building and Environment*. 2018; 142: 11–21. doi: 10.1016/j.buildenv.2018.06.003

16. Slimani Z, Trabelsi A, Virgone J, et al. Study of the Hygrothermal Behavior of Wood Fiber Insulation Subjected to Non-Isothermal Loading. *Applied Sciences*. 2019; 9(11): 2359. doi: 10.3390/app9112359
17. Latif E, Lawrence RMH, Shea AD, et al. An experimental investigation into the comparative hygrothermal performance of wall panels incorporating wood fibre, mineral wool and hemp-lime. *Energy and Buildings*. 2018; 165: 76–91. doi: 10.1016/j.enbuild.2018.01.028
18. Seng B, Magniont C, Gallego S, et al. Behavior of a hemp-based concrete wall under dynamic thermal and hygric solicitations. *Energy and Buildings*. 2021; 232: 110669. doi: 10.1016/j.enbuild.2020.110669
19. Chennouf N, Agoudjil B, Alioua T, et al. Experimental investigation on hygrothermal performance of a bio-based wall made of cement mortar filled with date palm fibers. *Energy and Buildings*. 2019; 202: 109413. doi: 10.1016/j.enbuild.2019.109413
20. Rahim M, Douzane O, Tran Le AD, et al. Experimental investigation of hygrothermal behavior of two bio-based building envelopes. *Energy and Buildings*. 2017; 139: 608–615. doi: 10.1016/j.enbuild.2017.01.058
21. Alioua T, Agoudjil B, Chennouf N, et al. Investigation on heat and moisture transfer in bio-based building wall with consideration of the hysteresis effect. *Building and Environment*. 2019; 163: 106333. doi: 10.1016/j.buildenv.2019.106333
22. Dong W, Chen Y, Bao Y, et al. A validation of dynamic hygrothermal model with coupled heat and moisture transfer in porous building materials and envelopes. *Journal of Building Engineering*. 2020; 32: 101484. doi: 10.1016/j.job.2020.101484
23. Kaoutari T, Louahlia H. Experimental and numerical investigations on the thermal and moisture transfer in green dual layer wall for building. *Case Studies in Thermal Engineering*. 2024; 53: 103946. doi: 10.1016/j.csite.2023.103946
24. Mendes N, Winkelmann F, Lamberts R, Philippi PC. Moisture effects on conduction loads. *Energy and buildings*. 2003; 35(7): 631–644.
25. Rouchier S, Busser T, Pailha M, et al. Hygric characterization of wood fiber insulation under uncertainty with dynamic measurements and Markov Chain Monte-Carlo algorithm. *Building and Environment*. 2017; 114: 129–139. doi: 10.1016/j.buildenv.2016.12.012
26. Dubois S, McGregor F, Evrard A, et al. An inverse modelling approach to estimate the hygric parameters of clay-based masonry during a Moisture Buffer Value test. *Building and Environment*. 2014; 81: 192–203. doi: 10.1016/j.buildenv.2014.06.018
27. Alioua T, Agoudjil B, Boudenne A, et al. Sensitivity analysis of transient heat and moisture transfer in a bio-based date palm concrete wall. *Building and Environment*. 2021; 202: 108019. doi: 10.1016/j.buildenv.2021.108019
28. Zhou Y, Trabelsi A, El Mankibi M. Hygrothermal properties of insulation materials from rice straw and natural binders for buildings. *Construction and Building Materials*. 2023; 372: 130770. doi: 10.1016/j.conbuildmat.2023.130770
29. Hagentoft CE. HAMSTAD—Final report: Methodology of HAM-modeling. Report R. 2002; 2 (8): 19–23.
30. Slimani Z. Experimental and numerical analysis of the hygrothermal behavior of highly hygroscopic walls (French). Lyon 1; 2015.
31. BS EN ISO 12571. Hygrothermal performance of building materials and products—Determination of hygroscopic sorption properties. British Standards Institution; 2013.
32. Künzle HM. Simultaneous heat and moisture transport in building components, One- and two-dimensional calculation using simple parameters. IRB-Verlag Stuttgart. 1995; 65.
33. Branco F, Tadeu A, Simões N. Heat conduction across double brick walls via BEM. *Building and Environment*. 2004; 39(1): 51–58. doi: 10.1016/j.buildenv.2003.08.005
34. Liu X, Chen Y, Ge H, et al. Numerical investigation for thermal performance of exterior walls of residential buildings with moisture transfer in hot summer and cold winter zone of China. *Energy and Buildings*. 2015; 93: 259–268. doi: 10.1016/j.enbuild.2015.02.016
35. Fang A, Chen Y, Wu L. Transient simulation of coupled heat and moisture transfer through multi-layer walls exposed to future climate in the hot and humid southern China area. *Sustainable Cities and Society*. 2020; 52: 101812. doi: 10.1016/j.scs.2019.101812
36. Hagentoft CE, Kalagasidis AS, Adl-Zarrabi B, et al. Assessment Method of Numerical Prediction Models for Combined Heat, Air and Moisture Transfer in Building Components: Benchmarks for One-dimensional Cases. *Journal of Thermal Envelope and Building Science*. 2004; 27(4): 327–352. doi: 10.1177/1097196304042436

37. Trabelsi A, Slimani Z, Virgone J. Response surface analysis of the dimensionless heat and mass transfer parameters of Medium Density Fiberboard. *International Journal of Heat and Mass Transfer*. 2018; 127: 623–630. doi: 10.1016/j.ijheatmasstransfer.2018.05.145
38. Eberhart R, Kennedy J. A new optimizer using particle swarm theory, *Micro Mach, Hum. Sci*; 1995.
39. Whitley D. A genetic algorithm tutorial. *Statistics and Computing*. 1994; 4(2): 65–85. doi: 10.1007/bf00175354
40. Chai T, Draxler RR. Root mean square error (RMSE) or mean absolute error (MAE), *Geoscientific Model Development Discussions*. 2014; 7(1): 1525–1534. doi: 10.5194/gmdd-7-1525-2014
41. Asan H. Numerical computation of time lags and decrement factors for different building materials. *Building and Environment*. 2006; 41(5): 615–620. doi: 10.1016/j.buildenv.2005.02.020
42. Rafidiarison H, Mougél E, Nicolas A. Laboratory experiments on hygrothermal behaviour of real-scale timber walls. *Maderas Ciencia y tecnología*. 2012; (ahead): 0-0. doi: 10.4067/s0718-221x2012005000010